Development of AFCAL: An Asteroid Flux Density Calculator for ALMA Observations

Shigeru Takahashi[1(✉)], Hikaru Kubota[2], Hideo Sagawa[1,3], Takashi Tsukagoshi[1,4], Fumi Yoshida[5,6], Junya Kawase[1], and Takahiro Iino[1]

[1] Information Technology Center, The University of Tokyo, 2-11-16 Yayoi, Bunkyo-ku, Tokyo 113-8658, Japan
{shigeru.takahashi,iino.takahiro}@mail.u-tokyo.ac.jp, j.kawase@ds.itc.u-tokyo.ac.jp

[2] Division of Science, Graduate School, Kyoto Sangyo University, Kamigamo Motoyama, Kita, Kyoto 603-8555, Japan
i2485049@cc.kyoto-su.ac.jp

[3] Faculty of Science, Kyoto Sangyo University, Kamigamo Motoyama, Kita, Kyoto 603-8555, Japan
sagawa@cc.kyoto-su.ac.jp

[4] Department of Innovative Engineering, Faculty of Engineering, Ashikaga University, 268-1 Omae-cho, Ashikaga 326-8558, Tochigi, Japan
takashi.tsukagoshi.astro@gmail.com

[5] University of Occupational and Environmental Health, Japan, 1-1 Iseigaoka, Yahata, Kitakyusyu 807-8555, Fukuoka, Japan
fumi-yoshida@med.uoeh-u.ac.jp

[6] Planetary Exploration Research Center, Chiba Institute of Technology, 2-17-1 Tsudanuma, Narashino, Chiba 275-0016, Japan

Abstract. We developed AFCAL (An Asteroid Flux Density Calculator for ALMA Observations), Python-based software designed to simulate the brightness temperature and radio flux of asteroids using thermophysical modeling (TPM) calculations. AFCAL numerically solves the heat conduction equation while accounting for thermal radiation from subsurface layers, enabling accurate simulations. By utilizing multiprocessing, AFCAL efficiently performs TPM calculations for each facet of a polygonal-shaped model, fully leveraging all CPU cores for faster computation.

We validate AFCAL using ALMA observations of the dwarf planet (1) Ceres. Additionally, we present simulation results for the asteroid (3200) Phaethon, the target of Japan's upcoming asteroid exploration mission. AFCAL enhances the interpretation of ALMA observations, contributing to a deeper understanding of asteroid thermal properties and supporting future research in planetary science.

Keywords: Asteroid · ALMA · Thermal Radiation · Numerical Simulation

© The Author(s), under exclusive license to Springer Nature Switzerland AG 2026
O. Gervasi et al. (Eds.): ICCSA 2025 Workshops, LNCS 15890, pp. 3–19, 2026.
https://doi.org/10.1007/978-3-031-97606-3_1

1 Introduction

Asteroids are considered primordial bodies that have undergone minimal thermal evolution compared to the major planets and retain relatively more information about the formation of the solar system. Therefore, the study of asteroids is indispensable for understanding the history of the solar system. Research on asteroids has been conducted from various perspectives, theoretical, observational studies, laboratory experiments and in-situ observations by spacecraft (e.g., [12]). In observational studies, research has mainly focused on the visible to mid-infrared wavelength ranges using ground-based telescopes and obtained numerous significant results.

On the other hand, observations of asteroids in the radio wavelength range, such as submillimeter and millimeter waves, have been relatively scarce. Two primary reasons for this are: (1) since asteroids' thermal emission in the radio wavelength ranges is lower compared to the mid-infrared, observations have been done for relatively large asteroids; (2) Models for describing thermal emission in the radio wavelength range were not sufficiently developed.

However, the advent of large aperture telescopes such as ALMA (Atacama Large Millimeter/submillimeter Array) has become possible to observe smaller bodies in the solar system (e.g., [2,8]). ALMA has solved the problems of the past, especially the observation sensitivity problem caused by (1) above, and made it possible to observe even smaller asteroids.

In order to promote more effective observational studies of asteroids using ALMA, the above mentioned problem (2), i.e., the lack of a thermal emission model of asteroids in the radio wavelength, has become a recent issue.

This study aims to develop software to calculate the radio intensity of asteroids for ALMA. The software will be based on an asteroid thermal emission model that integrates physical parameters required for the radio wavelength range.

2 Thermophysical Model (TPM)

Asteroidal thermal radiation arises from the process in which absorbed solar radiation is re-emitted as thermal energy. The intensity of this radiation is an essential tool for investigating the physical properties of asteroids and can be inferred from their surface temperatures. The temperature of an asteroid is determined by three primary physical processes: (1) absorption of solar radiation (mainly in the visible spectrum), (2) thermal re-emission in the infrared and radio wavelengths, and (3) heat conduction into the subsurface. Most asteroids are not composed of bare rock surfaces but are instead covered by regolith, a fine-grained rocky material that influences all of the above described three thermal processes. Therefore, studying an asteroid's thermal radiation allows us to estimate the physical parameters of its regolith, such as thermal conductivity, specific heat, and density.

A fundamental thermal model used to describe asteroid thermal radiation is the Standard Thermal Model (STM). This model assumes: (1) the asteroid

is either non-rotating or rotating very rapidly, (2) the nighttime temperature is zero, (3) there is no subsurface heat conduction, and (4) an empirical beaming factor η is used to correct for surface roughness effects. STM was successfully employed in creating a catalog of asteroid diameters and albedos based on infrared data from the IRAS satellite [1].

However, since actual asteroids rotate, the temperature of a given surface point varies throughout the day, decreasing at night as it radiates away stored heat. To accurately determine asteroid diameters from thermal radiation, it is essential to consider rotational effects. Thus, the Thermophysical Model (TPM) was developed, incorporating both rotation and subsurface heat conduction (e.g., see Delbo et al. in [12].

2.1 1D Conductive Heat Flow Equation

The TPM framework follows the approach outlined by Spencer et al. (1989) [18]. Considering a sufficiently small region of an asteroid's surface relative to its diameter, heat conduction can be treated as a one-dimensional process. This requires that the polygonal surface elements in TPM are small compared to the asteroid's diameter. The heat conduction equation is expressed as:

$$\frac{\partial T(z,t)}{\partial t} = \frac{k}{\rho c}\frac{\partial^2 T(z,t)}{\partial z^2}, \tag{1}$$

where $T(z,t)$ is the temperature at depth z and time t, ρ is the material density, c is the specific heat capacity, k is the thermal conductivity.

Although in reality, ρ may vary with depth and both c and k may depend on temperature, the TPM in this study assumes them to be constant values.

The thermal inertia Γ is defined as:

$$\Gamma = \sqrt{k\rho c}, \tag{2}$$

and has a unit $[\mathrm{Jm^{-2}s^{-0.5}K^{-1}}] \equiv$ tiu. This parameter represents the resistance of a material to temperature changes. A low thermal inertia asteroid exhibits large day-night temperature variations, whereas a high thermal inertia asteroid stores and releases heat more gradually, reducing diurnal temperature fluctuations. Generally speaking, regolith has low thermal inertia, while solid rock has high thermal inertia.

Defining the thermal skin depth l_s as:

$$l_s = \sqrt{\frac{k}{\rho c \omega}}, \tag{3}$$

where ω is the rotational angular velocity [rad/s], l_s represents the depth at which temperature variations decay to $1/e$ of their surface values.

2.2 Surface Boundary Condition

In the basic TPM, the energy balance at the asteroid surface is given by:

$$k\left(\frac{\partial T(z,t)}{\partial z}\right)_{z=0} = \epsilon\sigma T^4(0,t) - (1-A)F_s(t), \tag{4}$$

where the left-hand term represents subsurface heat conduction, and the right-hand terms include $\epsilon\sigma T^4(0,t)$: thermal radiation following Stefan-Boltzmann's law, $(1-A)F_s(t)$: absorbed solar energy, ϵ: emissivity, σ: the Stefan-Boltzmann constant and A: the Bond albedo. The solar flux received by a surface element is given by:

$$F_s(t) = S_0 \cdot \frac{1}{r(t)^2} \cdot \cos\theta(t), \tag{5}$$

where S_0 is the solar constant at 1 AU (1361 W/m^2), $r(t)$ is the asteroid's distance from the Sun (AU) and $\theta(t)$ is the solar incidence angle.

A rough surface creates shadowing and thermal re-radiation effects. To account for these, a surface roughness correction factor X is introduced as follows:

$$S_0(1-A)\cos\theta/r^2 = X\sigma T^4 + k\frac{\partial T}{\partial z}, \tag{6}$$

where $X = (1-\epsilon\xi)\epsilon$, with ξ being the roughness parameter [3]. It is noted that the NASA Dawn mission applied this model to determine thermal inertia values for the mean surface and some specific craters of Ceres (e.g., Haulani and Occator craters) [16]).

2.3 Internal Boundary Condition

For the asteroid interior, the deep subsurface is assumed to maintain a constant temperature beyond a depth d. Since we confirmed no temperature variation was observed for $d > 10 \cdot l_s$, we set $d = 20 \cdot l_s$ in this study:

$$\left(\frac{\partial T(z,t)}{\partial z}\right)_{z=d} = 0. \tag{7}$$

No internal heat flux is assumed.

2.4 Subsurface Thermal Radiation (STR)

The above model effectively calculates thermal radiation intensity in the mid-infrared to far-infrared wavelength range. However, observations at millimeter and submillimeter wavelengths have revealed lower observed temperatures than those predicted by this model [15]. This discrepancy is attributed to the exclusion of subsurface thermal radiation (STR) in the millimeter and submillimeter regimes [9]. Since electromagnetic waves in these wavelength ranges partially penetrate asteroid material, STR must also be considered. Consequently, several studies have incorporated this approach into their models (e.g., [4,5,10]).

Total Transmissivity. Thermal radiation from the subsurface is described using the complex dielectric permittivity $\tilde{\varepsilon}$ (or the complex refractive index $\tilde{n}$). If the constituent material is non-magnetic and non-conductive, the relationship between complex dielectric permittivity $\tilde{\varepsilon} = \varepsilon_1 + i\varepsilon_2$ and complex refractive index $\tilde{n} = n + i\kappa$ is given by:

$$\tilde{\varepsilon} = \tilde{n}^2, \quad \varepsilon_1 = n^2 - \kappa^2, \quad \varepsilon_2 = 2n\kappa, \tag{8}$$

$$n = \sqrt{\frac{|\tilde{\varepsilon}| + \varepsilon_1}{2}}, \quad \kappa = \sqrt{\frac{|\tilde{\varepsilon}| - \varepsilon_1}{2}}. \tag{9}$$

In addition, the loss tangent ($\tan\delta$) is often used in simulations to quantify energy dissipation in dielectric materials. It is defined as the ratio of the imaginary part to the real part of the permittivity:

$$\tan\delta = \frac{\varepsilon_2}{\varepsilon_1}. \tag{10}$$

Thermal radiation from the subsurface refracts and reflects at the asteroid surface. Given an incident angle θ_i within the asteroid and an exit angle θ_t into space, Snell's law applies:

$$n \sin\theta_i = \sin\theta_t. \tag{11}$$

Using Fresnel's equations, the reflection and transmission coefficients are derived. The reflection coefficients for s-polarized (r_s) and p-polarized (r_p) waves are:

$$r_s = \frac{n\cos\theta_i - \cos\theta_t}{n\cos\theta_i + \cos\theta_t}, \quad r_p = \frac{\cos\theta_i - n\cos\theta_t}{\cos\theta_i + n\cos\theta_t}. \tag{12}$$

The reflectance R_s and R_p are given by:

$$R_s = |r_s|^2, \quad R_p = |r_p|^2. \tag{13}$$

The total reflectance R is the mean of R_s and R_p:

$$R = \frac{R_s + R_p}{2}. \tag{14}$$

Similarly, the transmission coefficients for s-polarized (T_s) and p-polarized (T_p) waves are:

$$T_s = \left(\frac{2n\cos\theta_i}{n\cos\theta_i + \cos\theta_t}\right)^2, \quad T_p = \left(\frac{2\cos\theta_i}{\cos\theta_i + n\cos\theta_t}\right)^2. \tag{15}$$

The total transmissivity T_{tr} is given by:

$$T_{tr} = \frac{T_s + T_p}{2}. \tag{16}$$

By the principle of energy conservation, the relationship between total transmissivity and reflectance is:

$$T_{tr} + R = 1. \tag{17}$$

Electrical Skin Depth. Thermal radiation generated in the subsurface is attenuated as it propagates to the surface due to absorption by the internal material. The characteristic distance over which this attenuation occurs is called the electrical skin depth δ_{elec}, given by:

$$\delta_{elec} = \frac{\lambda}{4\pi\kappa}. \tag{18}$$

Flux Density (Intensity). With the above model, the surface and subsurface temperature distribution of the asteroid can be determined. The brightness temperature T_B observed from a given facet is computed using the Rayleigh-Jeans approximation by integrating the subsurface temperature profile $T(z)$ along the propagation direction;

$$T_B = (1 - R) \int T(z) \exp\left(-\frac{z}{\delta_{\text{elec}} \cos\theta_i}\right) \frac{dz}{\delta_{\text{elec}} \cos\theta_i}. \tag{19}$$

For an asteroid subtending a solid angle Ω as seen by the observer, the total observed flux density (intensity per unit frequency) I is:

$$I = \int_{\Omega} I_\nu \, d\Omega = \int_{\Omega} B_\nu(T) \, d\Omega. \tag{20}$$

In radio astronomy, the unit Jansky (Jy) is commonly used to measure radio flux density:

$$1 \text{ Jy} = 10^{-26} \text{ W m}^{-2} \text{ Hz}^{-1}. \tag{21}$$

Since asteroid thermal emission is a continuum spectrum, assuming that the spectral intensity remains approximately constant within the instrumental bandwidth BW, the observed intensity I_{obs} is expressed as:

$$I_{obs} = I \cdot BW. \tag{22}$$

3 Simulation

3.1 Overview

The AFCAL is developed using Python 3.11.5. To achieve efficient and high-precision calculations, it utilizes the numerical computation libraries *NumPy* and *SciPy*. For visualization of results, the graphing library *Matplotlib* is employed. AFCAL performs calculations on the high-performance computing system **mdx (a platform for building data-empowered society)** provided by the Information Technology Center at the University of Tokyo. The mdx is equipped with Intel Xeon Platinum 8368 CPUs and NVIDIA A100 Tensor Core GPUs. In this study, we used the Xeon CPUs for all computations. However, AFCAL is not restricted to the mdx and can be executed on any platform where Python 3.11.5 and the aforementioned modules are available, including Windows, macOS, Linux and Unix.

The calculation flow of AFCAL consists of six steps (Fig. 1). Here, we explain each step in detail.

3.2 Data Set Input

This step involves loading and pre-processing the input data set required for calculations.

Polygon Model. In AFCAL, asteroid shapes are modeled using polygon meshes. The model shapes are based on data provided by DAMIT (Database of Asteroid Models from Inversion Techniques) [6]. DAMIT is a database of asteroid shape models operated and managed by the Faculty of Mathematics and Physics at Charles University in the Czech Republic[1]. The shape models in DAMIT are derived by inverting asteroid lightcurve data. The database includes hundreds of asteroid models, each containing detailed information about their shape, rotational axis, and spin period. The format of DAMIT's shape models is a custom format but is similar to the Wavefront OBJ format. Additionally, the orientation of asteroid rotational axes is also provided by the same database. In this study, we use the models of (1) Ceres and (3200) Phaethon for the calculations.

Ephemeris. The ephemeris for asteroids is obtained from the Horizons System provided by NASA's Jet Propulsion Laboratory (JPL)[2]. The Horizons System is a tool that provides information on orbital elements, positions and velocities, apparent brightness, distances, and more for celestial bodies such as major planets, asteroids and comets within the solar system. It is widely used in scientific research, astronomical observations, and educational activities.

Data can be obtained via a web interface, email, telnet, and an API interface using HTTP GET and POST methods. In this study, the position information of asteroids at calculation times was obtained by interpolating values from prepared ephemeris.

3.3 Initial Preparation

We perform the rotation calculations to align the polygon with the spin axis. Additionally, we calculate the normal vectors of the facets for each rotational phase.

Rotation of Asteroids. Since asteroids rotate, it is necessary to perform polygon rotation calculations. Methods for rotation calculations include using matrices or Euler angles, but in this study, quaternions were used.

Quaternions are an extension of complex numbers and are expressed as follows:

$$q = w + xi + yj + zk, \tag{23}$$

[1] https://astro.troja.mff.cuni.cz/projects/damit/.
[2] https://ssd.jpl.nasa.gov/horizons/.

where w, x, y, z are real components, and i, j, k are imaginary units with the following properties:

$$i^2 = j^2 = k^2 = ijk = -1, \tag{24}$$

$$ij = k, \quad jk = i, \quad ki = j, \tag{25}$$

$$ji = -k, \quad kj = -i, \quad ik = -j. \tag{26}$$

Quaternions are widely used in computer graphics because they can represent rotations in three-dimensional space concisely and efficiently.

To rotate a three-dimensional vector $\mathbf{v}$ around an axis $\mathbf{u} = (u_x, u_y, u_z)$ by an angle θ, a unit quaternion q is defined as follows:

$$q = \cos\frac{\theta}{2} + \sin\frac{\theta}{2}(u_x i + u_y j + u_z k). \tag{27}$$

To rotate the vector $\mathbf{v}$ using the quaternion q, represent $\mathbf{v}$ as a pure imaginary quaternion and compute as follows:

$$\mathbf{v}' = q\mathbf{v}q^{-1}, \tag{28}$$

where q^{-1} is the inverse of quaternion q, and $\mathbf{v}'$ is the quaternion representing the rotated vector.

3.4 Initial TPM Calculation

Initial Condition. We obtain the initial temperature distribution of the asteroid as follows. First, the asteroid was fixed at the position of the initial calculation time (t_0), and the surface and internal temperatures were uniformly set to $T = 0$ K. Starting from this initial state, TPM calculation was done. The TPM calculation method will be described in the next section.

As the number of rotations increased, the temperature distribution stabilized and converged over time. In this simulation, the asteroid was rotated typically 100–1000 times to confirm that the temperature distribution had sufficiently converged. The resulting stable temperature distribution was adopted as the initial condition at the start of the calculation.

In AFCAL, numerical calculations of heat conduction are performed for multiple surface elements (polygons). For models with a large number of polygons, single-threaded calculations are computationally expensive and time-consuming. To address this, AFCAL employs Python's robust parallel processing module, *multiprocessing*.

By utilizing *multiprocessing*, AFCAL generates multiple processes, each of which independently handling the calculations for specific surface elements. This approach fully utilizes all available CPU cores, achieving significant acceleration through parallel computing.

3.5 TPM Calculation

TPM simulations are conducted, refining thermal models based on the results from the initial calculations as changing geometric parameters of the asteroid.

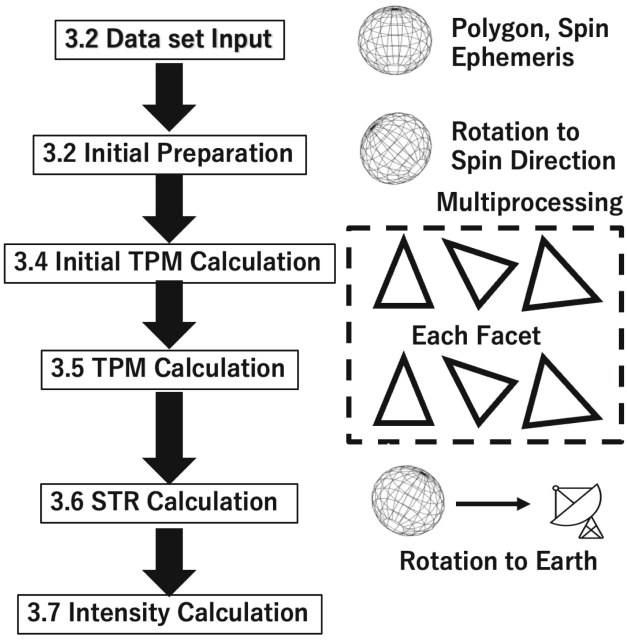

Fig. 1. Calculation Sequence of AFCAL.

1D Conductive Heat Flow Equation. An explicit finite difference method was used to solve the one-dimensional heat conduction equation. The finite difference equation is as follows:

$$T_i^{j+1} = T_i^j + \frac{\alpha \Delta t}{\Delta z^2} \left(T_{i+1}^j - 2T_i^j + T_{i-1}^j \right), \tag{29}$$

where:

- T_i^j: Temperature at spatial position $z = i\Delta z$ and time $t = j\Delta t$
- Δz: Spatial step size
- Δt: Time step size
- α: Thermal diffusivity
- $i = 0, 1, 2, \ldots, N$: Spatial index
- $j = 0, 1, 2, \ldots$: Time index

Introducing the parameter:

$$r = \frac{\alpha \Delta t}{\Delta z^2}. \tag{30}$$

The partial differential equation can be rewritten as:

$$T_i^{j+1} = T_i^j + r \left(T_{i+1}^j - 2T_i^j + T_{i-1}^j \right). \tag{31}$$

For stability in the explicit method, the following condition must be satisfied:

$$r = \frac{\alpha \Delta t}{\Delta z^2} \leq \frac{1}{2}. \tag{32}$$

Since the above equation cannot determine T_0^{j+1} and T_N^{j+1}, the following boundary conditions are used:

For the asteroid's interior:

$$T_{N-1}^{j+1} = T_N^{j+1}. \tag{33}$$

For the asteroid's surface, the boundary condition in finite difference form is:

$$\left(\frac{\partial T}{\partial z}\right)_{z=0} = \frac{1}{\Delta z}\left(T_1^{j+1} - T_0^{j+1}\right). \tag{34}$$

Thus:

$$T_0^j = T_1^j - \frac{1}{k}\left[X\sigma\left(T_0^j\right)^4 - (1-A)F(t)\right]\Delta z. \tag{35}$$

To solve this equation and obtain T_0^{j+1}, several methods such as self-consistent method can be used. In this study, Newton-Raphson method was adopted.

3.6 STR Calculation

To calculate STR as observed from Earth, the polygonal shape model was rotated toward Earth. Then, the STR for each facet was calculated using Eq. (19). Numerical integration was required for Eq. (19). Since the function decreases exponentially, Gauss-Laguerre Quadrature was used for the calculation.

3.7 Flux Density (Intensity) Calculation

In this step, the final flux density (intensity) values are calculated based on the previous calculations. Using Eq. (20), the STR (Spectral Thermal Radiation) from each facet is summed to determine the observed intensity. Additionally, visualize the asteroid's shape and temperature distribution at the time of observation and create an animation.

4 Results

4.1 (1) Ceres

(1) Ceres is the largest dwarf planet located in the main asteroid belt of the solar system. It orbits the Sun at an average distance of approximately 2.8 AU (4.2×10^8 km) and completes one revolution around the Sun in about 4.6 years (see Fig. 2). Additionally, Ceres rotates on its axis approximately every

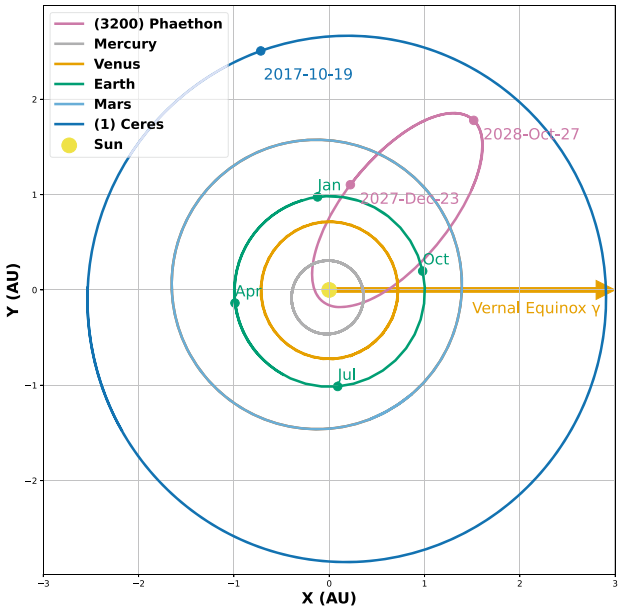

Fig. 2. Orbital Diagram of Planets, (1) Ceres and (3200) Phaethon.

9 h (Russell et al., 2016). Its shape closely resembles a triaxial ellipsoid, with principal radii of $a = 483.1$ km, $b = 481$ km, and $c = 445.9$ km, giving it an almost spherical structure [17].

Detailed observations by NASA's Dawn spacecraft revealed that the surface of Ceres contains partially bright regions. Around the Occator Crater, transient hazes have been reported [13], suggesting that Ceres is a relatively active celestial body. Moreover, (1) Ceres is sometimes used as a calibrator (reference source) in ALMA observations.

In this software, validation was performed by comparing the results with ALMA observations conducted on October 19, 2017. (1) Ceres was observed using ALMA Band 6 (1.1 mm, 265 GHz), and physical parameters such as thermal inertia and dielectric permittivity were estimated [10]. The used parameters are summarized in Table 1 and the results are shown in Fig. 3. Figure 3a shows the distribution of brightness temperature when observed in the mid-infrared and Fig. 3b the calculated distribution of brightness temperature when observed with ALMA Band 6.

The brightness temperature observed by ALMA on October 19, 2017, was 179 ± 5 K, and the radio intensity was 1.60 ± 0.05 Jy. In comparison, the calculated results were 173 K and 1.62 Jy, which is approximately 1 K lower than the observational value. However, in the simulation the brightness temperature varies between 172 K and 174 K due to rotational effects during the observation period. Therefore, the calculation results are considered to be in good agreement with the observational data. In the mid-infrared calculations, the average

Table 1. Physical Parameters Used for the Calculation of (1) Ceres

Parameter	Value	Reference/Comment
Facet number	800	DAMIT
Shape (a,b,c)	(482.64×480.64×445.57) km	Russell et al. (2016) [17]
Rotation Period	9.074170 hr	Chamberlain et al. (2007)
Pole direction (λ,β)	(11°, 81°)	Park et al. (2016) [14]
Emissivity ϵ	0.95	Keihm et al. (2013) [9]
Bond albedo A	0.037	Li et al. (2019) [11]
Roughness parameter ξ	0.0	Lambertian scattering
Thermal inertia Γ	80 tiu	Li et al. (2020) [10]
Dielectric constant ϵ_r	2.25	Li et al. (2020) [10]
Loss tangent tanδ	0.03	Li et al. (2020) [10]
Frequency f_{rq}	264.985 GHz	ALMA Observation [10]

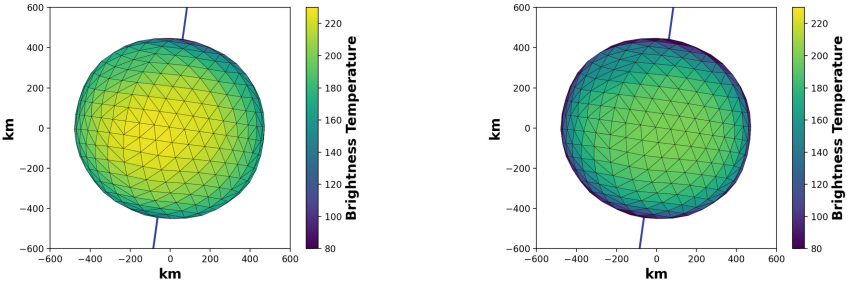

(a) (b)

Fig. 3. (a) Calculated Surface Temperature of (1) Ceres, (b) Calculated Brightness Temperature Considering STR for (1) Ceres.

brightness temperature was 200 K, and the intensity was 1.88 Jy. In contrast, the brightness temperature observed in ALMA Band 6 was approximately 27 K lower and the intensity was 0.26 Jy lower, representing a difference of about 15%.

This decrease in observed temperature can be influenced by various factors such as thermal inertia, and complex dielectric permittivity etc. Although the same 15% decrease may not be observed for other asteroids, this value would serve as a useful reference.

4.2 (3200) Phaethon

(3200) Phaethon is an asteroid with an approximate diameter of 5 km and a rotation period of about 3.6 h. It has a highly eccentric elliptical orbit, with a perihelion distance of 0.14 AU (∼21 million km) and an aphelion distance of 2.4

AU (∼360 million km). This distinctive orbit brings (3200) Phaethon closer to the Sun than Mercury's orbit and farther than Mars' orbit.

Moreover, (3200) Phaethon is classified as a Near-Earth Object (NEO) and is known as the parent body of the Geminid meteor shower. To investigate this peculiar asteroid in more detail, JAXA is planning an exploration mission to (3200) Phaethon with the Deep Space Exploration Technology Demonstrator (DESTINY$^+$) spacecraft[3]. Research on the thermophysical parameters of (3200) Phaethon is limited, but its thermal inertia is estimated to be $\Gamma = 600 \pm 200$ tiu [7]. In this study, we used this value, while other physical parameters were assumed to be the same as those for (1) Ceres (Table 2).

For the Roughness parameter (ξ), the value $\xi = 0.55$ observed at the Occator Crater on (1) Ceres was used [16]. This choice was made because the Occator Crater has a higher thermal inertia ($\Gamma = 115$ - 136 tiu) compared to other regions on Ceres. However, it should be noted that this choice is not based on theoretical or observational reason for (3200) Phaethon possesses this same roughness value.

Table 2. Physical Parameters Used for the Calculation of (3200) Phaethon

Parameter	Value	Reference/Comment
Facet number	2040	DAMIT
Diameter	5.1 km	Hanuš et al. 2016 [7]
Rotation Period	3.603957 hr	DAMIT
Pole direction (λ,β)	(318°, −47°)	DAMIT
Emissivity ϵ	0.95	Substituting the value used for (1) Ceres
Bond Albedo A	0.048	Hanuš et al. 2016 [7]
Roughness parameter ξ	0.55	Substituting the value used for Occator Crater
Thermal inertia Γ	600 tiu	Hanuš et al. 2016 [7]
Dielectric constant ϵ_r	2.25	Substituting the value used for (1) Ceres
Loss tangent $\tan\delta$	0.03	Substituting the value used for (1) Ceres
Frequency f_{rq}	264.985 GHz	ALMA Observation

We investigated the brightness temperature and radio intensity of (3200) Phaethon at two distinct orbital positions; closest approach to Earth on December 23 and near aphelion on October 27, 2028 (Fig. 4). The brightness temperature on December 23, 2027 was calculated to be 280 K, and the radio intensity was 7.4 mJy (Fig. 4a). Conversely, near aphelion on October 27, 2028, the brightness temperature was estimated to be 199 K, with the radio intensity of 169 μJy (Fig. 4b). We also confirmed that the uncertainty of ±200 in the thermal inertia of (3200) Phaethon leads to only about a $1-2\%$ variation in the brightness temperature. These calculations reveal a significant intensity difference by a factor of approximately 44 between the two orbital positions.

[3] https://www.perc.it-chiba.ac.jp/en/projects/destiny-plus/.

This variation in brightness temperature and intensity is attributed to the substantial change in the heliocentric distance of (3200) Phaethon along its highly elliptical orbit. When Phaethon approaches the Sun, the surface temperature increases, resulting in higher brightness temperature and radio intensity. Conversely, as it moves away from the Sun towards aphelion, the surface temperature decreases, leading to lower observed values.

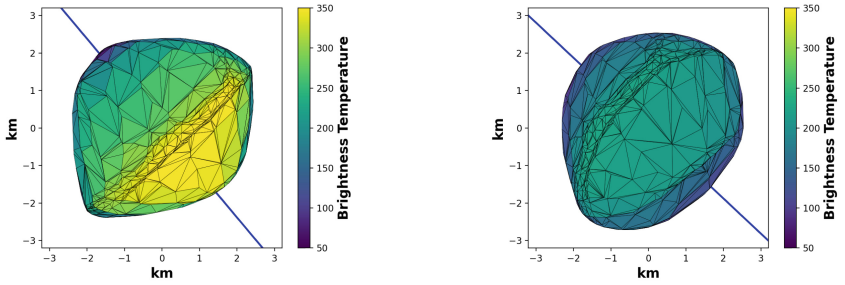

(a) 2027-Dec-23 (b) 2028-Oct-27

Fig. 4. Brightness Temperature and Apparent Shape Variations of (3200) Phaethon at Different Positions: (a) during closest approach to Earth, (b) at aphelion.

This information is particularly valuable for planning future observations, including those by the DESTINY$^+$ mission.

5 Evaluation of Parallelization in AFCAL

We evaluated the performance of parallelization in AFCAL (Asteroid Flux Calculator for ALMA), using Python's `multiprocessing` module to run radiative transfer calculations.

To assess scalability, we defined the parallel speedup as:

$$s(p) = \frac{t(1)}{t(p)}.$$

The test case was based on the dwarf planet (1) Ceres, and the execution time using a single processor was measured as $t(1) = 4.98$ h. The results are shown in Fig. 5. The ideal linear speedup is also plotted for comparison.

Assuming software-related factors dominate the overhead, we applied Amdahl's law. From the maximum speedup $s_{\max} \approx 55$, the parallelizable fraction was estimated as:

$$f = 1 - \frac{1}{s_{\max}} \approx 0.982.$$

This indicates that about 98.2% of AFCAL's computation can be parallelized. Further improvements will depend on reducing the remaining serial components such as I/O and initialization.

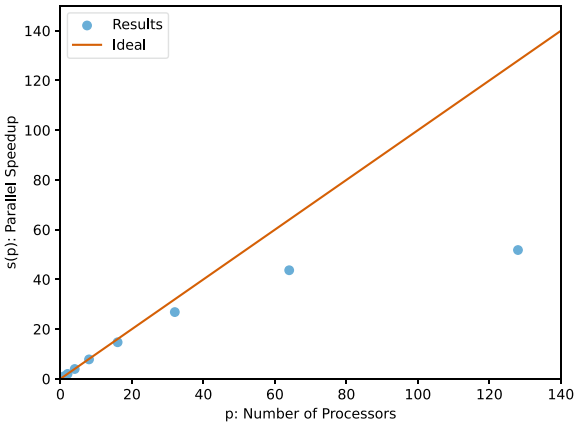

Fig. 5. Measured speedup $s(p)$ as a function of processor count p, compared with ideal scaling, for the case of (1) Ceres.

6 Future Prospects

The current implementation of AFCAL has demonstrated high parallel efficiency. However, further improvements in total computation time remain desirable, particularly when applying TPM to a large number of small bodies or high-resolution datasets.

A promising direction for future development lies in the adoption of novel algorithms. Zhao et al. (2024) [20] recently proposed an approach that applies a deep operator neural network to the computation of asteroid surface temperature. Their method achieved a reduction in computational cost by five orders of magnitude compared to traditional TPM techniques. Incorporating such algorithmic advances into AFCAL could offer substantial speedup and extend its applicability to real-time or large-scale modeling scenarios.

7 Summary

This study presents a thermophysical modeling software, AFCAL, developed using Python to simulate the brightness temperature and flux density of asteroids for millimeter and submillimeter wavelength observations, with a particular focus on ALMA. It simulates thermal radiation not only from the asteroid's surface but also from the subsurface layers. Additionally, the software utilizes Python's multiprocessing module to achieve high-speed and efficient parallel computing.

To validate the results of our developed software, we used ALMA Band 6 observational data of (1) Ceres from October 19, 2017. A comparison between the observational data and simulation results confirmed high accuracy and reliability in brightness temperature and flux density calculations. Furthermore, as a demonstration of the software's capability, brightness temperatures and flux

densities of (3200) Phaethon were calculated for two orbital positions: the closest approach to Earth and near aphelion. These simulations demonstrated the software's applicability to other asteroid observations.

Acknowledgments. The author would like to thank the three anonymous referees for their constructive and insightful comments. This research was supported by MEXT as "Developing a Research Data Ecosystem for the Promotion of Data-Driven Science" and as the JSPS Kakenhi (21H01142, 21H05420, 23K20872 and 24K07097). We used the "mdx: a platform for building data-empowered society" for the data analysis [19].

References

1. Asteroids. 2. Univ. of Arizona Pr, Tucson, Ariz (1989)
2. ALMA Partnership, Hunter, T.R., et al.: THE 2014 ALMA LONG BASELINE CAMPAIGN: OBSERVATIONS OF ASTEROID 3 JUNO AT 60 KILOMETER RESOLUTION. Astrophys. J. **808**(1), L2 (2015). https://doi.org/10.1088/2041-8205/808/1/L2
3. Davidsson, B.J., Gutiérrez, P.J., Rickman, H.: Physical properties of morphological units on Comet 9P/Tempel 1 derived from near-IR Deep Impact spectra. Icarus **201**(1), 335–357 (2009). https://doi.org/10.1016/j.icarus.2008.12.039
4. De Kleer, K., et al.: Ganymede's surface properties from millimeter and infrared thermal emission. Planet. Sci. J. **2**(1), 5 (2021). https://doi.org/10.3847/PSJ/abcbf4
5. De Kleer, K., Cambioni, S., Shepard, M.: The surface of (16) psyche from thermal emission and polarization mapping. Planet. Sci. J. **2**(4), 149 (2021). https://doi.org/10.3847/PSJ/ac01ec
6. Ďurech, J., Sidorin, V., Kaasalainen, M.: DAMIT: a database of asteroid models. Astron. Astrophys. **513**, A46 (2010). https://doi.org/10.1051/0004-6361/200912693
7. Hanuš, J., et al.: Near-Earth asteroid (3200) phaethon: characterization of its orbit, spin state, and thermophysical parameters. Astron. Astrophys. **592**, A34 (2016). https://doi.org/10.1051/0004-6361/201628666
8. Iino, T., Sagawa, H., Tsukagoshi, T., Nozawa, S.: A belt-like distribution of gaseous hydrogen cyanide on Neptune's equatorial stratosphere detected by ALMA. Astrophys. J. Lett. **903**(1), L1 (2020). https://doi.org/10.3847/2041-8213/abbb9a
9. Keihm, S., et al.: Reconciling main belt asteroid spectral flux density measurements with a self-consistent thermophysical model. Icarus **226**(1), 1086–1102 (2013). https://doi.org/10.1016/j.icarus.2013.07.005
10. Li, J.Y., Moullet, A., Titus, T.N., Hsieh, H.H., Sykes, M.V.: Disk-integrated thermal properties of ceres measured at millimeter wavelengths. Astron. J. **159**(5), 215 (2020). https://doi.org/10.3847/1538-3881/ab8305
11. Li, J.Y., et al.: Spectrophotometric modeling and mapping of Ceres. Icarus **322**, 144–167 (2019). https://doi.org/10.1016/j.icarus.2018.12.038
12. Michel, P., DeMeo, F.E., Bottke, W.F.: Asteroids IV. The University of Arizona Space Science Series, The University of Arizona press in collaboration with Lunar and planetary institute, Tucson (2015)
13. Nathues, A., et al.: Sublimation in bright spots on (1) Ceres. Nature **528**(7581), 237–240 (2015). https://doi.org/10.1038/nature15754

14. Park, R.S., et al.: A partially differentiated interior for (1) Ceres deduced from its gravity field and shape. Nature **537**(7621), 515–517 (2016). https://doi.org/10.1038/nature18955
15. Redman, R.O., Feldman, P.A., Matthews, H.E.: High-Quality photometry of asteroids at millimeter and submillimeter wavelengths. Astron. J. **116**(3), 1478–1490 (1998). https://doi.org/10.1086/300495
16. Rognini, E., et al.: High thermal inertia zones on ceres from dawn data. J. Geophys. Res. Planets **125**(3), e2018JE005733 (2020). https://doi.org/10.1029/2018JE005733
17. Russell, C.T., et al.: Dawn arrives at ceres: exploration of a small, volatile-rich world. Science **353**(6303), 1008–1010 (2016). https://doi.org/10.1126/science.aaf4219
18. Spencer, J.R., Lebofsky, L.A., Sykes, M.V.: Systematic biases in radiometric diameter determinations. Icarus **78**(2), 337–354 (1989). https://doi.org/10.1016/0019-1035(89)90182-6
19. Suzumura, T., eta l.: mdx: A cloud platform for supporting data science and cross-disciplinary research collaborations. In: 2022 IEEE International Conference on Dependable, Autonomic and Secure Computing, International Conference on Pervasive Intelligence and Computing, International Conference on Cloud and Big Data Computing, International Conference on Cyber Science and Technology Congress (DASC/PiCom/CBDCom/CyberSciTech), pp. 1–7 (2022). https://doi.org/10.1109/DASC/PiCom/CBDCom/Cy55231.2022.9927975
20. Zhao, S., Lei, H., Shi, X.: Deep operator neural network applied to efficient computation of asteroid surface temperature and the Yarkovsky effect. Astron. Astrophys. **691**, A224 (2024). https://doi.org/10.1051/0004-6361/202451789